Supplementary Information

Dual-defect surface engineering of bimetallic sulfide nanotubes towards flexible asymmetric solid-state supercapacitors

Experimental section

Synthesis of P-NiCo$_2$S$_4$

All the reagents purchased from Aladdin were of analytical grade and used without further purification. Prior to the experiment, the CF substrate was treated with concentrated HNO$_3$ solution for 1 h, then cleaned by deionized (DI) water for several times. In a typical synthesis, 1.5 mmol of Ni(NO$_3$)$_2$, 3 mmol of Co(NO$_3$)$_2$·6H$_2$O, and 10 mmol of CO(NH$_2$)$_2$ were dissolved in 40 mL of DI water and stirred to form a homogenous pink solution at room temperature. The obtained mixture and one piece of cleaned CF substrate (1.5 cm × 3.0 cm) were transferred to a Teflon-lined stainless-steel autoclave. The autoclave was sealed and kept at 120 °C for 8 h, and then allowed to cool to room temperature. The CF with the as-grown Ni-Co precursor nanowires were rinsed with DI water and dried at 60 °C for 12 h in a vacuum oven. Subsequently, the CF supported Ni-Co precursor nanowires were immersed into 0.2 M of Na$_2$S aqueous solution and then transferred to an autoclave and maintained at 160 °C for 10 h. The resulting NiCo$_2$S$_4$ nanotubes was washed with DI water and ethanol several times, and dried at 60 °C for 12 h in a vacuum oven. We performed an annealing process at 350 °C for 2 h under Ar to increase the crystallinity. The loading mass of the as-synthesized NiCo$_2$S$_4$ nanotubes on the CF substrate was ~3.6 mg cm^{-2}. To prepare P-NiCo$_2$S$_4$ nanotubes, a porcelain boat with NaH$_2$PO$_2$·H$_2$O (0.25 g) was placed at the upstream side of a tube furnace. The other porcelain boat loaded with NiCo$_2$S$_4$ nanowires were placed at the downstream side. The reaction was conducted at 350 °C for 2 h at a ramp rate of 5 °C min^{-1} under the flow of Ar gas. The loading mass of P-NiCo$_2$S$_4$ nanotubes on CF substrate was ~3.5 mg cm^{-2}.

For comparison, the NiCo$_2$S$_4$ samples were subjected by a similar phosphating strategy at the different amounts of P source (0.15 and 0.40 g), and the products were denoted

as P-NiCo$_2$S$_4$-1 and P-NiCo$_2$S$_4$-2, respectively.

Synthesis of P-NiCo$_2$S$_{4-x}$

The obtained P-NiCo$_2$S$_4$ nanotubes anchored on CF were immersed in a solution containing 30 mL of ethylene glycol and 30 mmol of NaOH and transferred to an autoclave for hydrothermal reaction at 120 °C for 12 h. Then, the substrate with P-NiCo$_2$S$_{4-x}$ nanotubes was taken out, washed with DI water and ethanol, and dried at 60 °C for 12 h in a vacuum oven. The average loading mass of P-NiCo$_2$S$_{4-x}$ on CF substrate was ~3.2 mg cm^{-2}. For comparison, NiCo$_2$S$_{4-x}$ was fabricated without phosphorization treatment and the loading mass was ~3.3 mg cm^{-2}. For comparison, the NiCo$_2$S$_4$ samples were subjected by different chemical reduction time (t_R = 6 and 12 h), and the products are denoted as NiCo$_2$S$_{4-x}$-1and NiCo$_2$S$_{4-x}$-2, respectively.

Synthesis of NiCo$_2$S$_{4-x}$-P

In order to explore the sequencing effect of the phosphating process and reduction process on electrochemical performance, the sample were fabricated following the inversible process, i.e., first reduction process then phosphorization treatment. The prepared sample, denoted as NiCo$_2$S$_{4-x}$-P, was prepared with the identical parameters of P-NiCo$_2$S$_{4-x}$, as previously stated.

Material characterization

The morphological characteristics and nanostructure of the samples were examined with a field-emission scanning electron microscope (FE-SEM Hitachi S4800) and a transmission electron microscope (TEM, JEM-2100F), respectively. The chemical composition and crystalline structures of samples were determined by X-ray diffractometry (XRD, Bruker D8) equipped with Cu Kα radiation (λ=1.5406 Å). Raman spectroscopy (Renishaw Invia) was performed at room temperature with a laser excitation of 532 nm. The surface chemical states of samples were analyzed by X-ray photoelectron spectroscopy (XPS, UltraDLD). The sulfur vacancy was determined by electron paramagnetic resonance (EPR, JEOL FA200) measurements. The Brunauer–Emmett–Teller (BET) specific surface areas were recorded with a micrometrics

apparatus (ASAP 2020 M) using liquid nitrogen as an adsorbent (77 K). The electrical conductivity of the sample slices compressed from as-synthesized powders were measured by a semiconductor characterization system (Keithley 4200-SCS) using a 4-probe method.

Theoretical calculation details

The density functional theory (DFT) calculations were performed using the Vienna ab initio simulation package (VASP).[1, 2] The generalized gradient approximation (GGA) with Perdew-Burke-Ernzerhof (PBE) exchange-correlation function was performed for all electronic energies of the exchange correlation.[3] The projector augmented wave (PAW) method was used to describe the interaction between core electrons and valence electrons.[4] The valence configurations include $3s^2 3p^3$ for P, $3s^2 3p^4$ for S, $3d^8 4s^1$ for Co and $3d^8 4s^2$ for Ni. A cut-off energy of 400 eV was adopted for the use of plane-wave basis set. The convergence criteria of self-consistent field (SCF) for maximum energy difference and residual force on atoms converge were reached at 10^{-5} eV and 0.05 eV/Å, respectively.[5] A Monkhorst-Pack grid of $3 \times 3 \times 3$ k-point mesh was conducted for structural optimization and density of states (DOS) calculation. Considering calculation simplicity, one S atom was removed from the unit cell and the P heteroatom replaces an S atom to model the structure of P-NiCo$_2$S$_{4-x}$.

Electrochemical measurements

The electrochemical measurements of the samples including the cyclic voltammetry (CV), galvanostatic charg–discharge (GCD), and electrochemical impedance spectroscopy (EIS) were conducted in a three-electrode configuration with a 2 M KOH aqueous electrolyte by an electrochemical workstation (CHI660E). The prepared samples (1×1 cm^2) were directly used as the working electrodes, a 5 mm × 5 mm platinum plate was used as the counter electrode, and the saturated calomel electrode (SCE) served as the reference electrode. The EIS tests were carried out in a frequency range from 100 kHz to 0.01 Hz at a stable open circuit voltage. The specific capacity (

Q_s, C g^{-1}) of P-NiCo$_2$S$_{4-x}$/CF electrodes were calculated from the discharge profiles using the following equations:[6]

$$Q_s = 2\frac{I\int_{t_i}^{t_f} V dt}{m\Delta V} \tag{1}$$

where I (A) is the discharge current density; t_i (s) and t_f (s) are the initial and final values of the discharge time, respectively; V (V) is the operating potential during the discharge process; m (g) is the loading mass; ΔV (V) is the potential window.

To further evaluate P-NiCo$_2$S$_{4-x}$/CF electrochemical performance, a flexible solid-state asymmetric supercapacitor (ASC) was assembled. The electrochemical tests of the ASC devices were conducted on a two-electrode cell with P-NiCo$_2$S$_{4-x}$/CF as positive electrode and activated carbon (AC, YP50F)/CF as negative electrode. The gel electrolyte of polyvinyl alcohol (PVA)/KOH was prepared using a previously reported method.[1] The AC/CF electrodes were prepared by mixing 80 wt% of AC, 15 wt% of acetylene black and 5 wt% of polyvinylidene fluoride and then coated onto a CF substrate. According to the charge balance between positive and negative electrodes, the mass loading of AC was calculated by the following formula:

$$\frac{m_+}{m_-} = \frac{C_{s-} \times \Delta V_-}{Q_{s+}} \tag{2}$$

where C_{s-} (F g^{-1}) and ΔV_- are the specific capacitance and the potential window of AC/CF in three-electrode testing system, respectively.

The specific capacitance (C_d, F g^{-1}), specific capacity (Q_d), energy density (E, W h kg^{-1}), power density (P, W kg^{-1}) and coulombic efficiency (η) of the ASC device were calculated using the following equations: [7, 8]

$$C_d = 2\frac{I_d\int_0^{\Delta t} V_d dt}{M\Delta V_d^2} \tag{3}$$

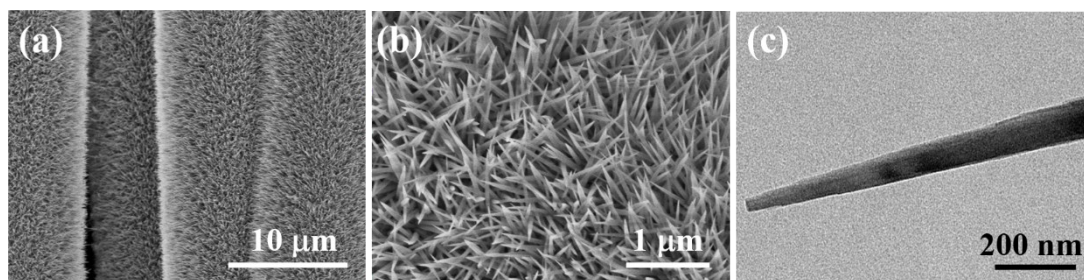$$Q_d = 2\frac{I_d\int_0^{\Delta t} V_d dt}{MV_d} \tag{4}$$

$$E = \frac{I_d \int_0^{\Delta t} V_d dt}{3.6 \times M} \tag{5}$$

$$P = \frac{3600 \times E}{\Delta t} \tag{6}$$

$$\eta = \frac{C_d}{C_c} \times 100\% \tag{7}$$

Where I_d (A) is the discharge current; Δt (s) is the discharge time; V_d (V) is the operating potential; ΔV_d (V) is the potential window of the discharge process; M (g) is the total mass of the active materials in both electrodes, and C_c (F g^{-1}) is the charge specific capacitance.
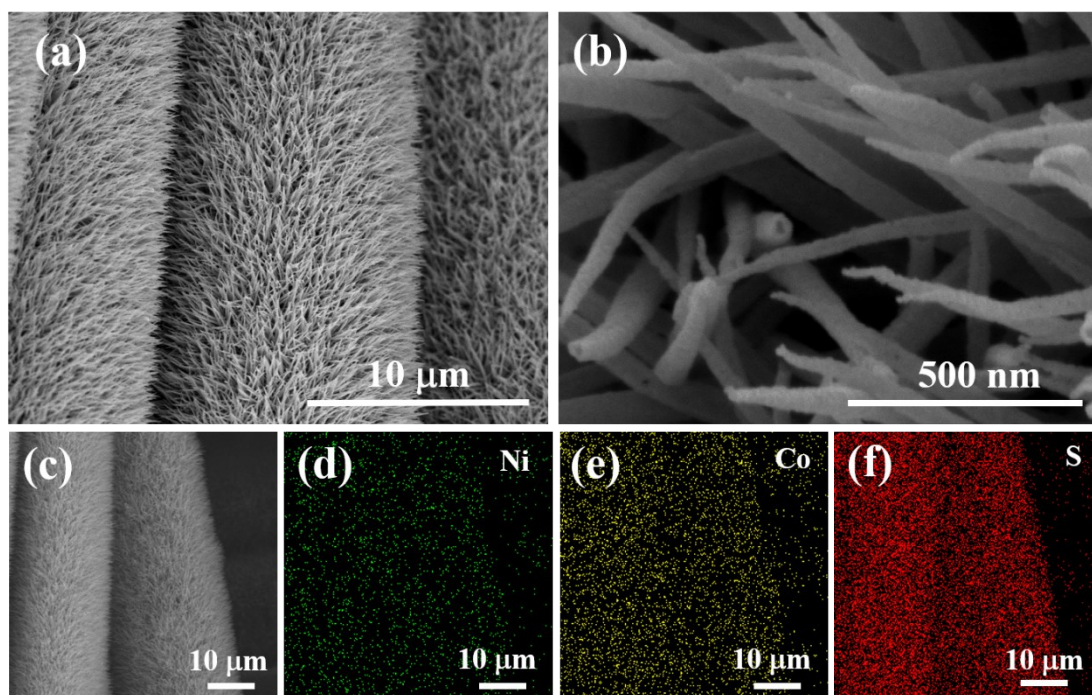
Fig. S1. (a, b) SEM images of the NiCo precursor nanowires at different magnifications.

(c)TEM image of an individual nanowire for NiCo precursor.
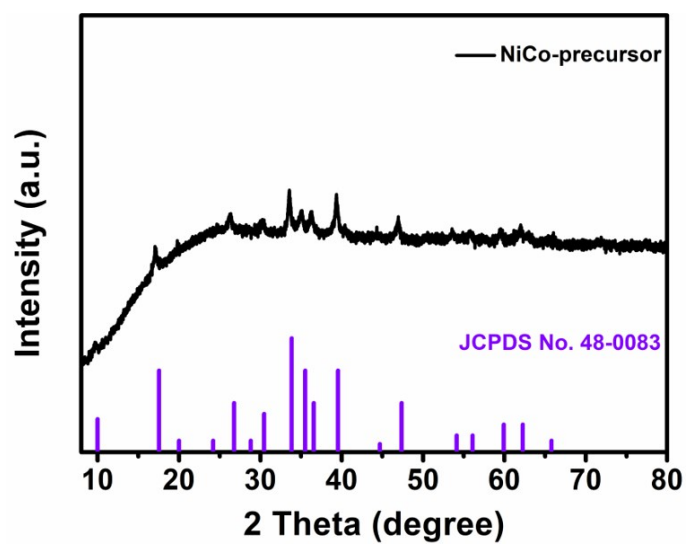
Fig. S2. The XRD spectrum of NiCo precursor

Fig. S3. (a, b) SEM images of the NiCo$_2$S$_4$ nanotubes at different magnifications and

(c–f) corresponding SEM-EDS mapping results.
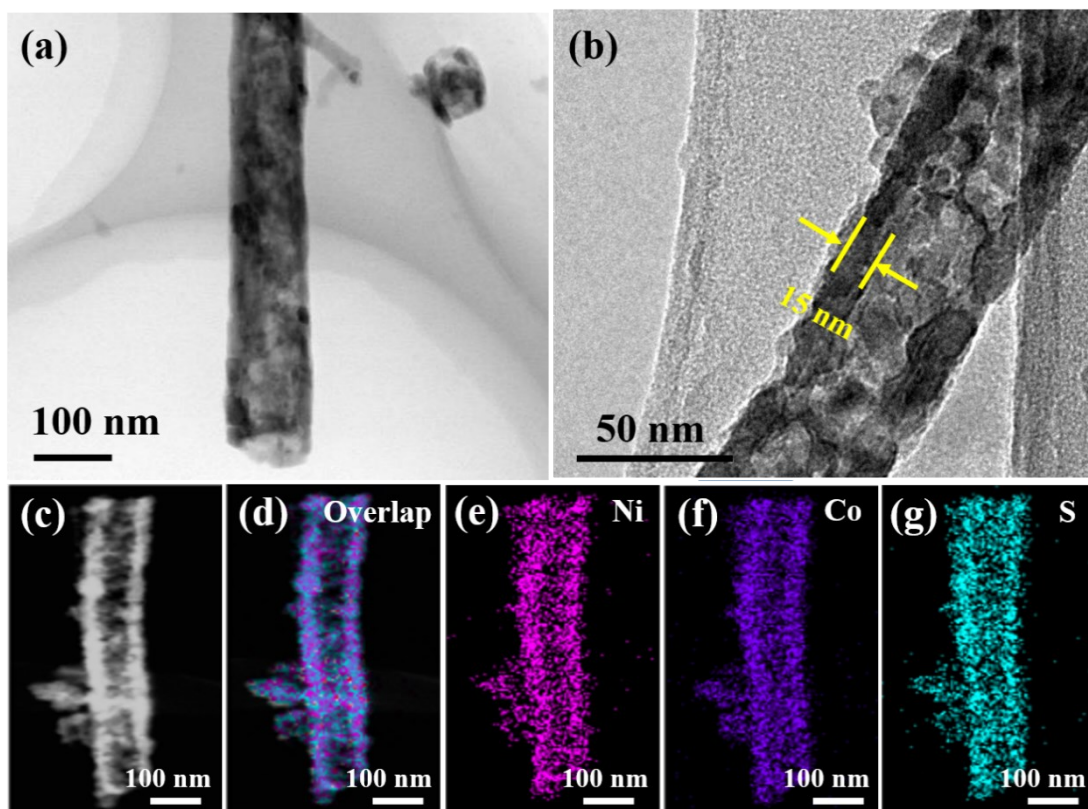
Fig. S4. (a, b) TEM images of the NiCo$_2$S$_4$ nanotubes and (c–g) EDX mapping images of the different elements of Ni, Co, and S recorded from an individual nanotube for NiCo$_2$S$_4$.

Element	Wt%	Atomic%
Ni	5.34	5.09
Co	11.34	10.72
S	11.84	20.81
C	35.27	22.62
Cu	26.09	40.76
Total:	100.00	100.00

Fig. S5. EDS spectrum of NiCo$_2$S$_4$ nanotube (the inset table shows the corresponding atomic contents).
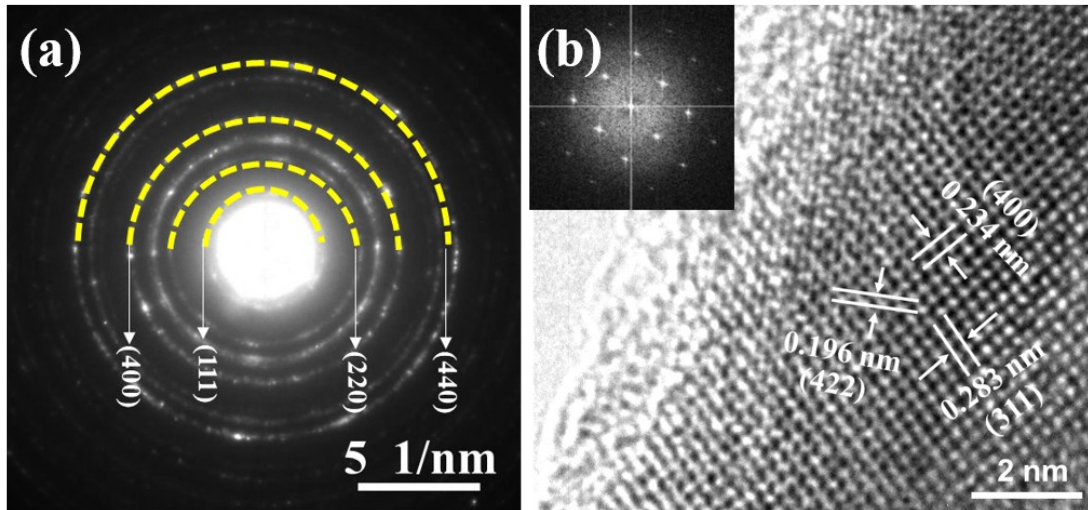
Fig. S6. (a) SAED image and HRTEM image of the NiCo$_2$S$_4$ nanotubes.
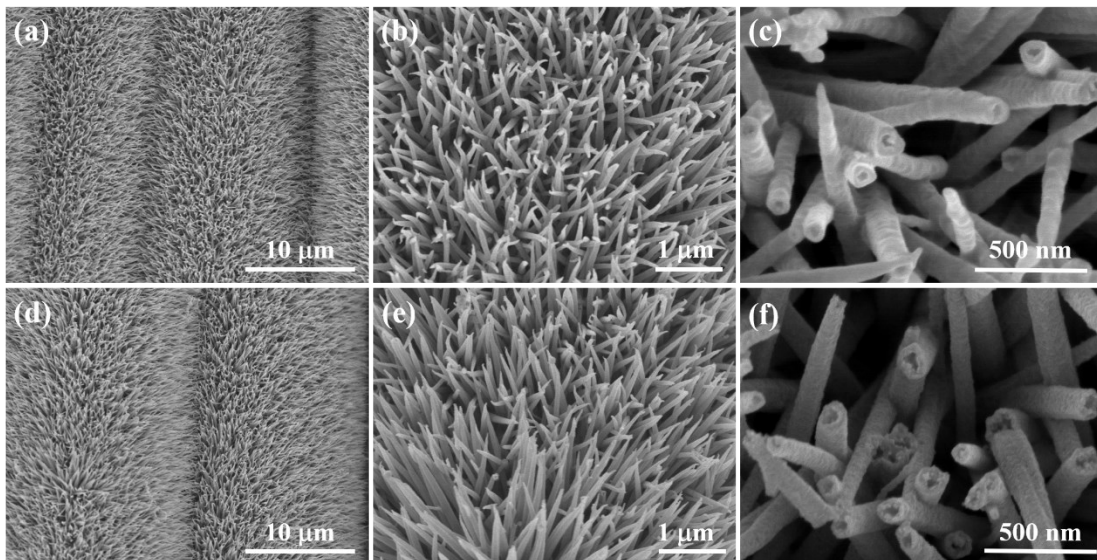
Fig. S7. SEM images for (a–c) P-NiCo$_2$S$_4$ and (d–f) NiCo$_2$S$_{4-x}$ obtained at different magnifications.
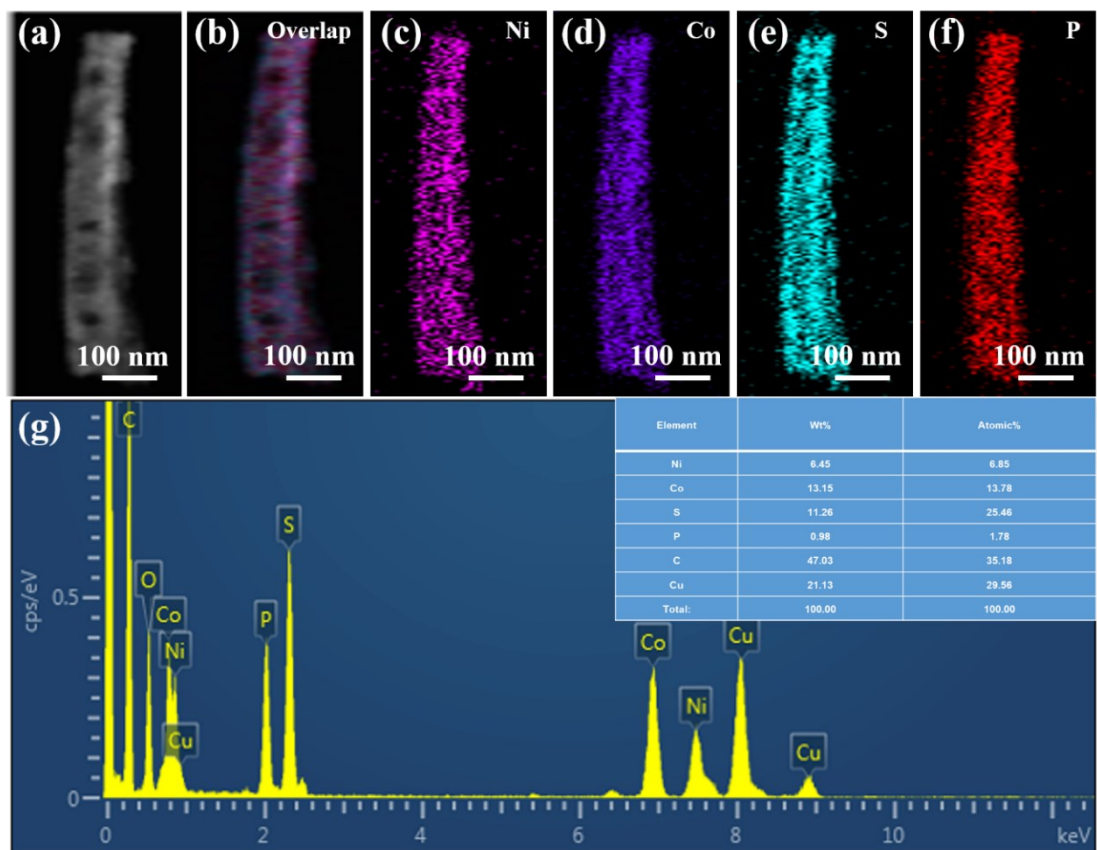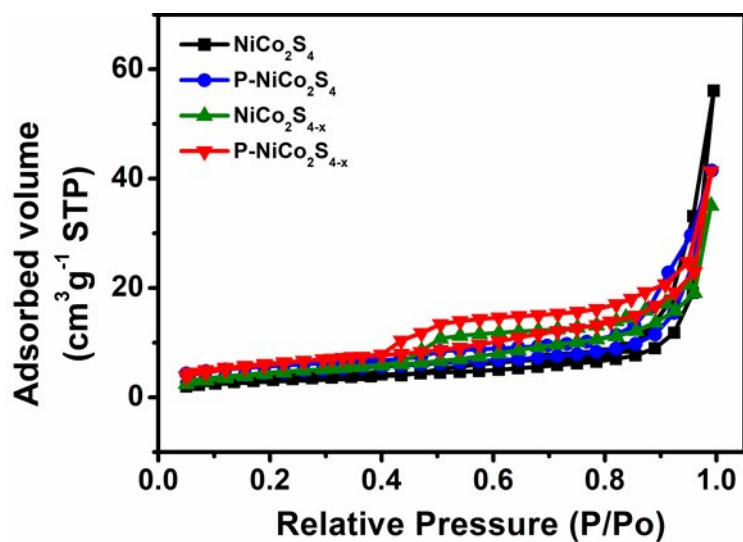
Fig. S8. (a) STEM image of the P-NiCo$_2$S$_4$ nanotube; (b–f) EDX mapping images of the different elements of Ni, Co, S, and P recorded from an individual nanotube for P-NiCo$_2$S$_4$.
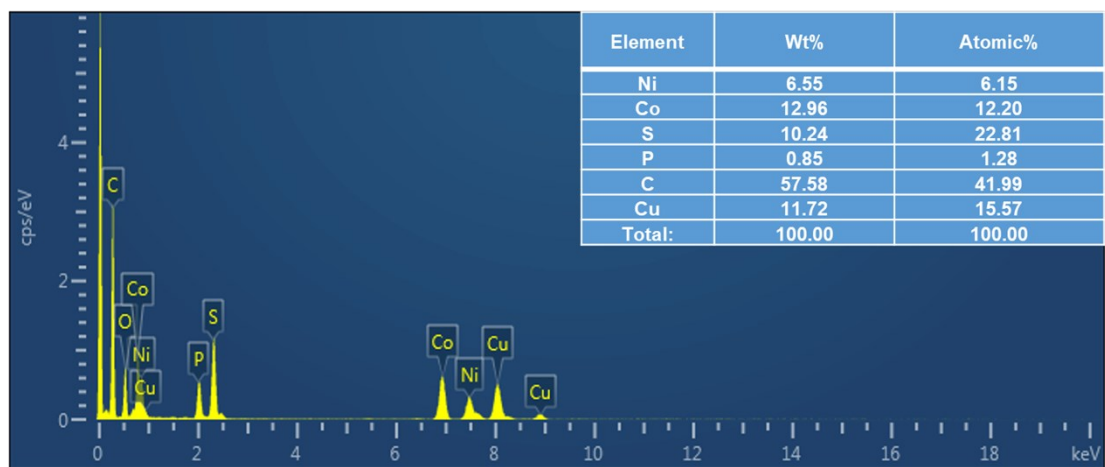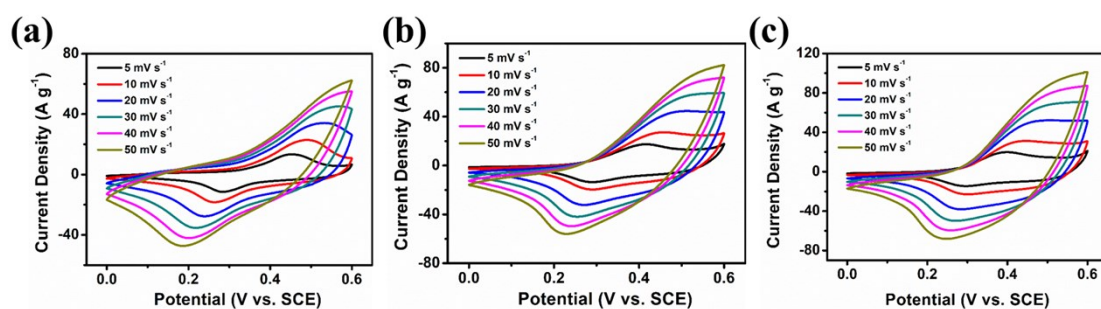

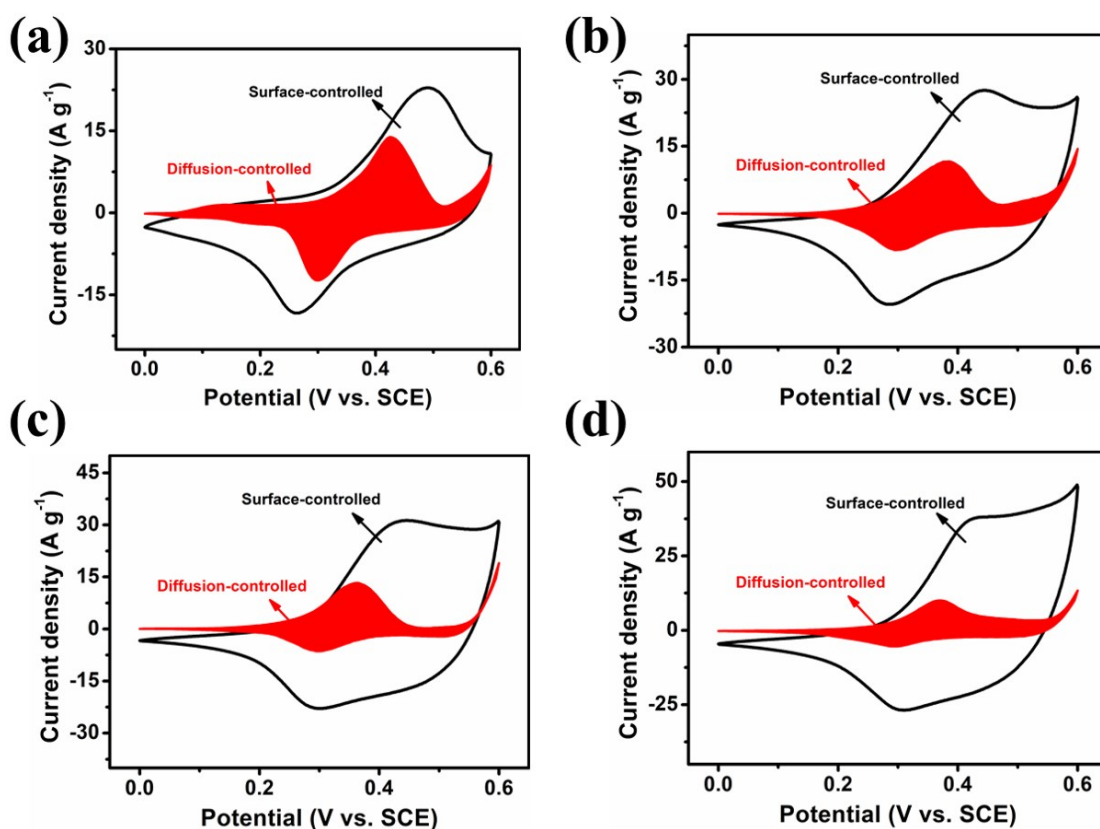**Fig. S9.** EDS spectrum of P-NiCo$_2$S$_{4-x}$ nanotube (the inset table shows the corresponding atomic contents).
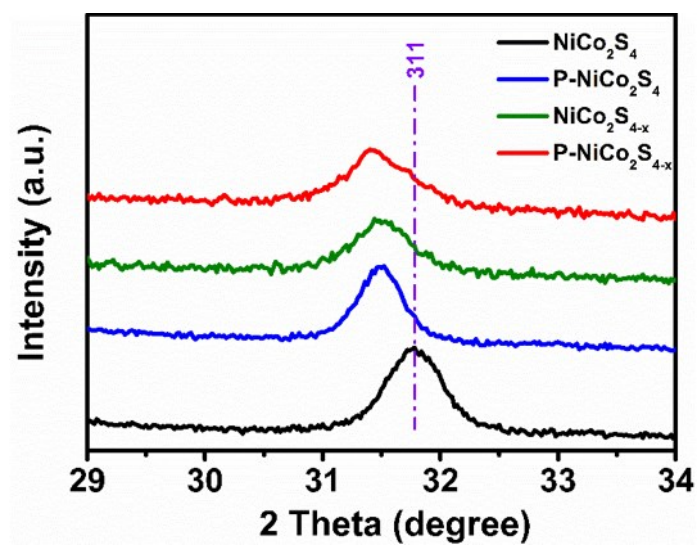
Fig. S10. Magnified view of the XRD (311) peak.

Fig. S11. The N_2 sorption isotherms of (a) $NiCo_2S_4$, (b) $P-NiCo_2S_4$, (c) $NiCo_2S_{4-x}$ and (d) $P-NiCo_2S_{4-x}$.

Fig. S12. CV curves of (a) $NiCo_2S_4$, (b) $P-NiCo_2S_4$, and (c) $NiCo_2S_{4-x}$ electrodes obtained at various scan rates.
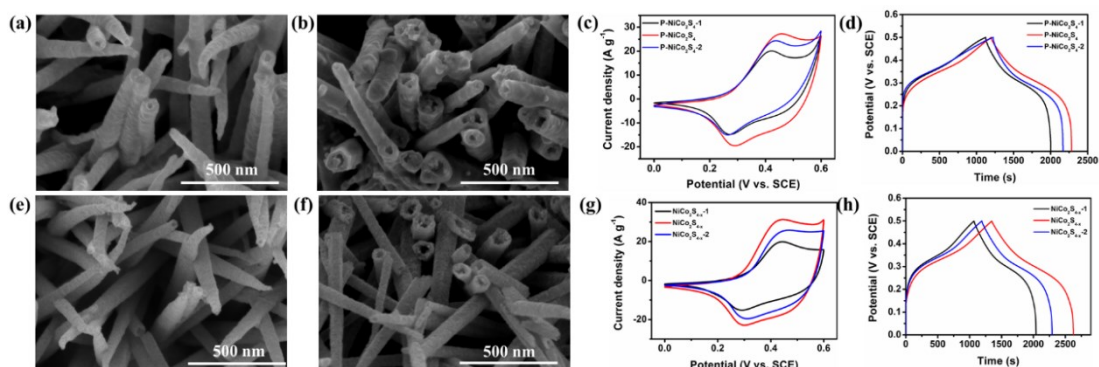
Fig. S13. The contribution of the surface-controlled process (the white area) and diffusion-controlled process (the red area) at a scan rate of 10 mV s^{-1} of (a) NiCo$_2$S$_4$, (b) P-NiCo$_2$S$_4$, (c) NiCo$_2$S$_{4-x}$ and (d) P-NiCo$_2$S$_{4-x}$ electrodes for the charge storage.
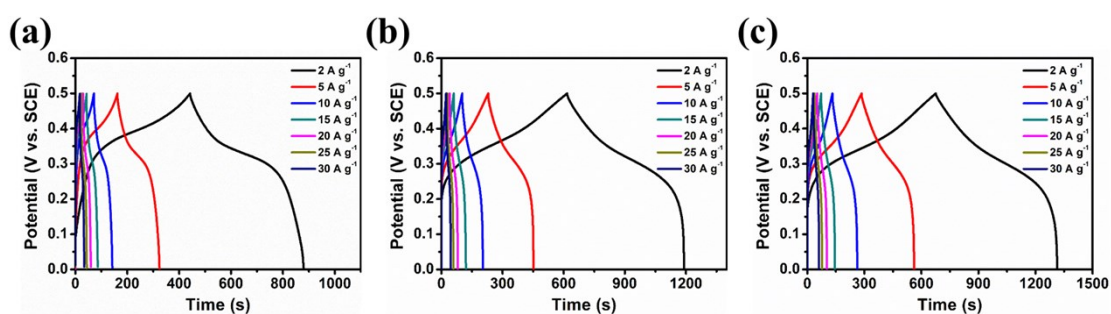
Fig. S14. GCD profiles of (a) NiCo$_2$S$_4$, (b) P-NiCo$_2$S$_4$, and (c) NiCo$_2$S$_{4-x}$ electrodes obtained at different current densities.

Fig. S15. (a) SEM image for P-NiCo$_2$S$_4$-1; (b) SEM image for P-NiCo$_2$S$_4$-2; (c) Comparison of the CV curves of P-NiCo$_2$S$_4$-1, P-NiCo$_2$S$_4$, and -NiCo$_2$S$_4$-2 at a scan rate of 10 mV s^{-1}; (d) Comparison of the GCD curves of P-NiCo$_2$S$_4$-1, P-NiCo$_2$S$_4$, and -NiCo$_2$S$_4$-2 at a current density of 1 A g^{-1}; (e) SEM image for NiCo$_2$S$_{4-x}$-1; (f) SEM image for NiCo$_2$S$_{4-x}$-2; (g) Comparison of the CV curves of NiCo$_2$S$_{4-x}$-1, NiCo$_2$S$_{4-x}$, and NiCo$_2$S$_{4-x}$ at a scan rate of 10 mV s^{-1}; (h) Comparison of the GCD curves of NiCo$_2$S$_{4-x}$-1, NiCo$_2$S$_{4-x}$, and NiCo$_2$S$_{4-x}$ at a current density of 1 A g^{-1}.

The P-NiCo$_2$S$_4$-1 sample prepared from a low dosage (0.15g) of P source displays a well-retained nanotube structure with rough surface (Fig. S15a). However, the nanotubes tend to agglomeration, since the P source dosage was increased to 0.40g (Fig. S15b). The CV curves (Fig. S15c) of P-NiCo$_2$S$_4$-1, P-NiCo$_2$S$_4$, and P-NiCo$_2$S$_4$-2 electrodes were obtained at a scan rate of 10 mV s^{-1}. And the NiCo$_2$S$_4$ electrode exhibits the largest CV integral area. Meanwhile, the GCD plots (Fig. S15d) collected at 1 A g^{-1} reveal that the P-NiCo$_2$S$_4$ electrode displays the longest discharge time. These results indicate that the optimized mass of P source used for phosphorization treatment is 0.25g.

The NiCo$_2$S$_{4-x}$-1 obtained by slight degree of reduction maintains the nanotube

structure well (Fig. S15e). However, the nanostructure of $NiCo_2S_{4-x}$-2 tends to structural collapse due to the degree of reduction increase (Fig. S15f). Fig. S15g and S15h depict the comparative CV and GCD curves of $NiCo_2S_{4-x}$-1, $NiCo_2S_{4-x}$, and $NiCo_2S_{4-x}$-2 electrodes, respectively. Remarkably, the $NiCo_2S_4$ electrode exhibits the largest CV integral area and longest discharge time, indicating the superior electrochemical performance. These results suggest that the optimized reduction time for solvothermal reduction is 12 h.
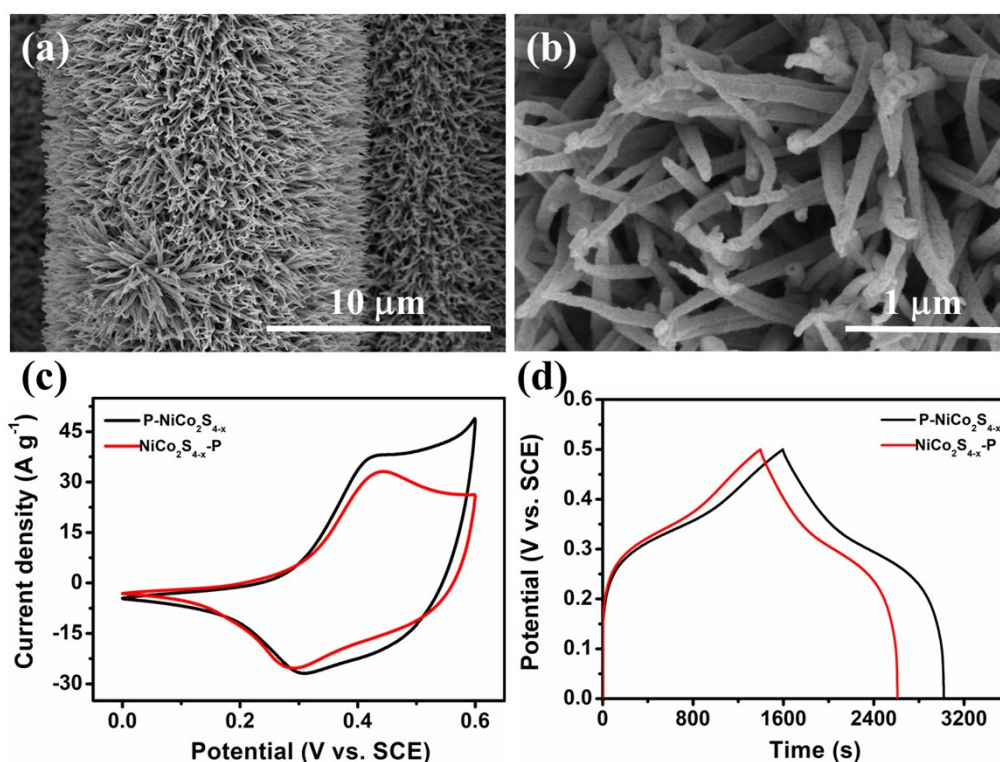
Fig. S16. (a, b) SEM images for $NiCo_2S_{4-x}$-P; (c) Comparison of the CV curves of $NiCo_2S_{4-x}$-P and P-$NiCo_2S_{4-x}$ at a scan rate of 10 mV s^{-1}; (d) Comparison of the GCD curves of $NiCo_2S_{4-x}$-P and P-$NiCo_2S_{4-x}$ at a current density of 1 A g^{-1};
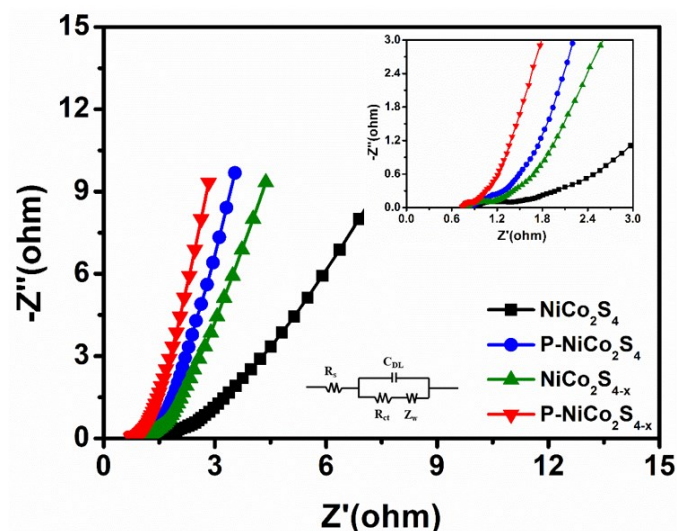
**Fig. S17.** Nyquist plots of (a) $NiCo_2S_4$, (b) $P-NiCo_2S_4$, (c) $NiCo_2S_{4-x}$ and (d) $P-NiCo_2S_{4-x}$ electrodes.
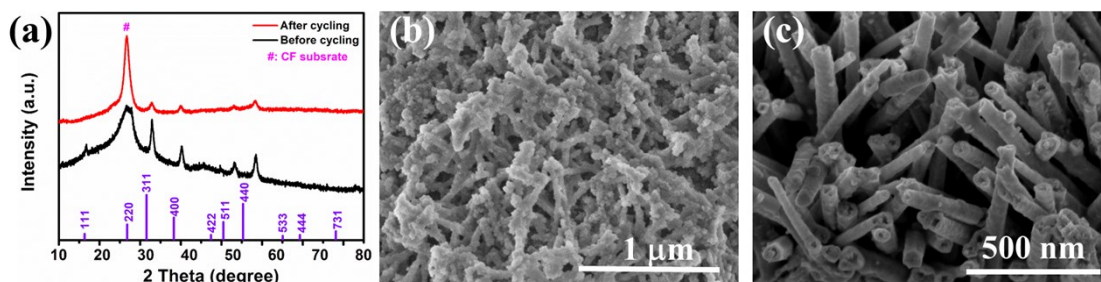
Fig. S18. (a) The comparative XRD spectra of $P-NiCo_2S_{4-x}$ before and after cycling test. (b, c) The SEM images for $P-NiCo_2S_{4-x}$ after cycling tests.

In Fig. S18a, the diffraction peak intensities of the $NiCo_2S_4$ become weak, and the FWHW of the diffraction peaks is increased, indicating the weakened crystallinity after cycling test. The (220) peak of $NiCo_2S_4$ at ~26.8° is close to the characteristic peak (located at ~26.2°) of carbon cloth. Thus, the diffraction peak of carbon cloth appeared prominent.
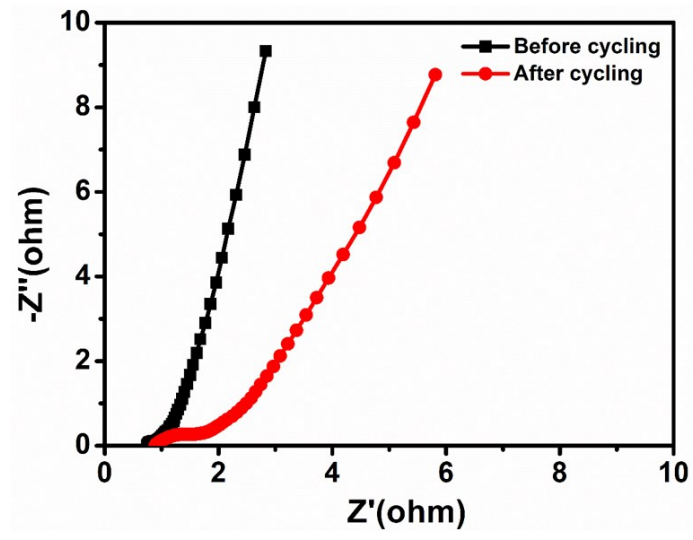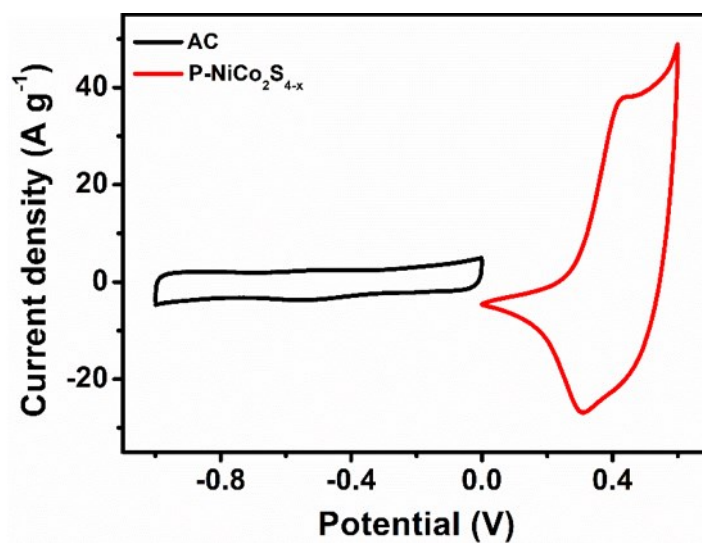
Fig. S19. Comparison of the EIS plots of P-NiCo$_2$S$_{4-x}$ electrode before and after undergoing the cycling tests.
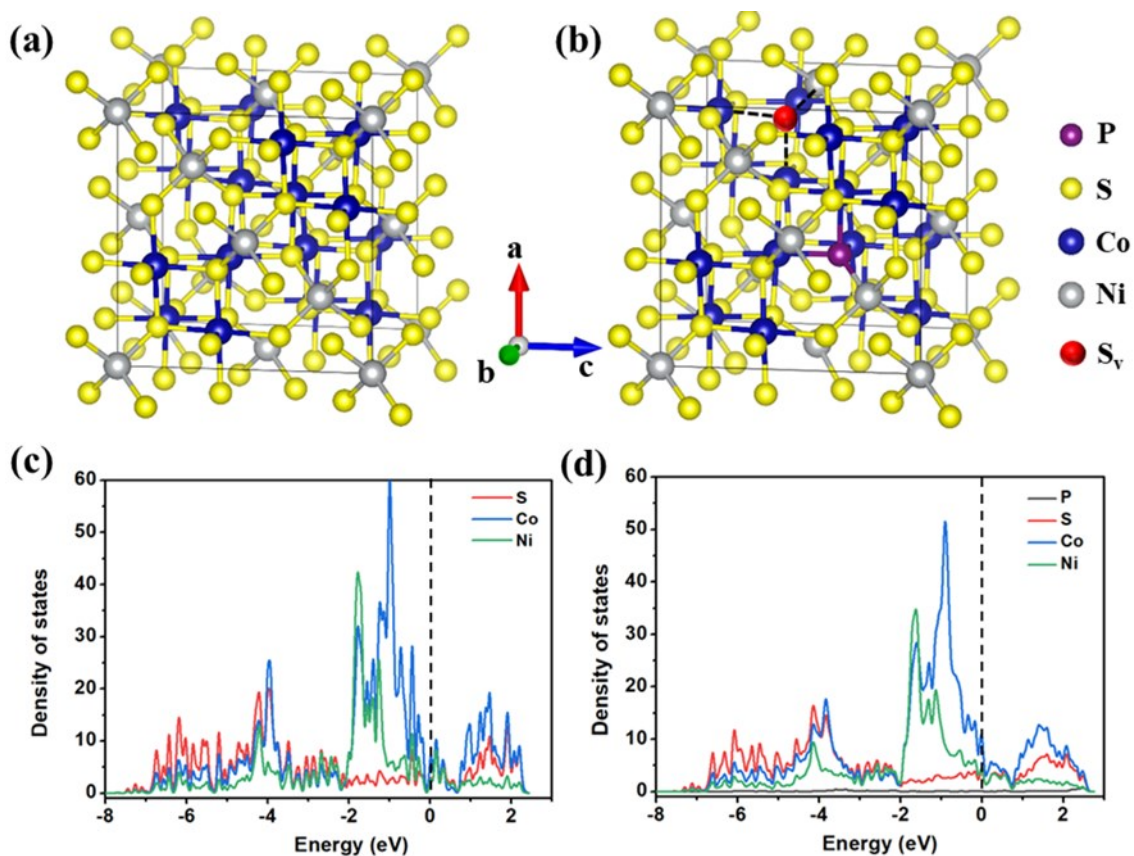
Fig. S20. Crystal structures of (a) $NiCo_2S_4$ and (b) $P-NiCo_2S_{4-x}$. The purple, yellow, blue, grey, and red spheres present P, S, Co, Ni and S vacancy (S_v), respectively. DOS plots of (c) $NiCo_2S_4$ and (d) $P-NiCo_2S_{4-x}$.

Fig. S21. Comparative CV curves obtained for AC and $F-CuCo_2S_{4-x}$ electrodes at a scan rate of 10 mV s^{-1}.
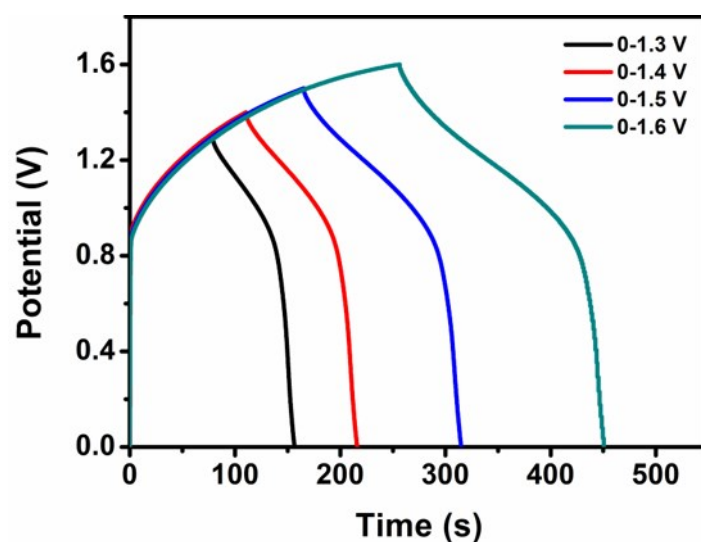
Fig. S22. The GCD profiles for P-NiCo$_2$S$_{4-x}$//AC ASC device recorded at different operating potentials at a current density of 1 A g^{-1}
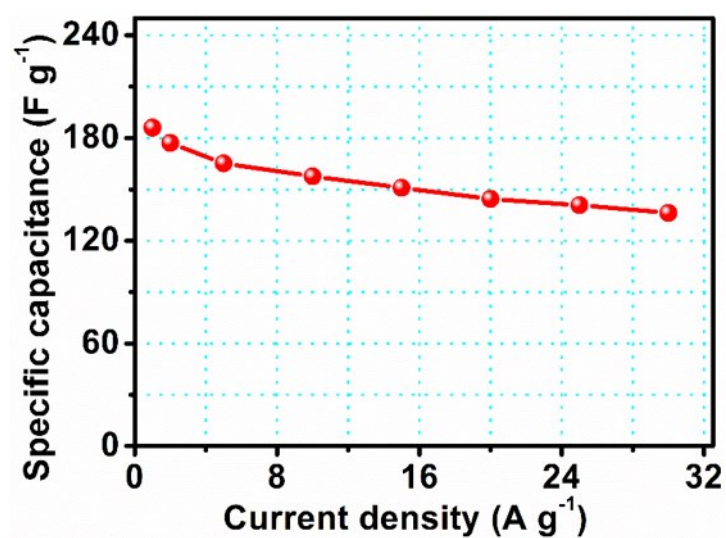
Fig. S23. Specific capacitance of the P-NiCo$_2$S$_{4-x}$//AC ASC device calculated from the GCD curves as a function of the current density.
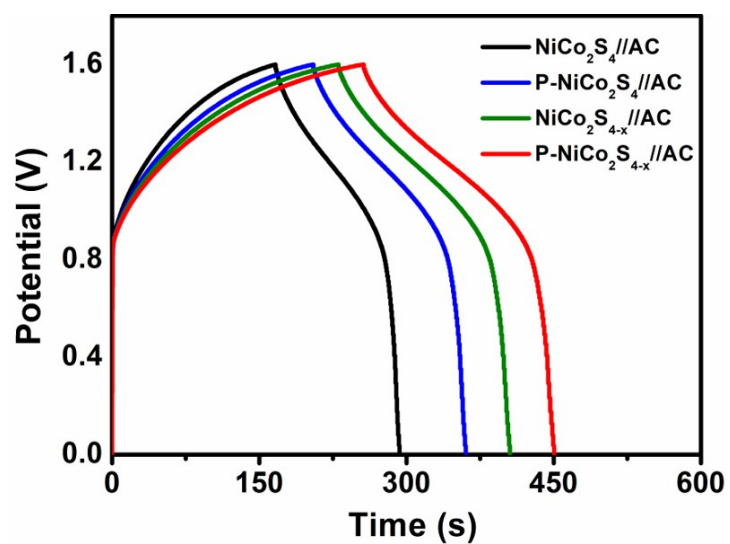
Fig. S24. GCD profiles of $NiCo_2S_4$//AC, P-$NiCo_2S_4$//AC, $NiCo_2S_{4-x}$//AC and P-$NiCo_2S_{4-x}$//AC recorded at a current density of 1 A g^{-1}.

Table S1. The lattice parameters of samples

Samples	a (Å)	b (Å)	c (Å)	V (Å3)
$NiCo_2S_4$	9.387	9.387	9.387	827.14
P-$NiCo_2S_4$	9.392	9.392	9.392	828.34
$NiCo_2S_{4-x}$	9.396	9.396	9.396	829.54
P-$NiCo_2S_{4-x}$	9.400	9.400	9.400	830.67

Table S2. The detailed information of Ni and Co elements for samples

Samples	Ni 2p$_{3/2}$ (eV)	Ni 2p$_{1/2}$ (eV)	Ni^{2+} Area	Ni^{3+} area	Ni^{2+}/Ni^{3+}	Co 2p$_{3/2}$ (eV)	Co 2p$_{1/2}$ (eV)	Co^{2+} area	Co^{3+} area	Co^{2+}/Co^{3+}
NiCo$_2$S$_4$	856.53	874.14	2121	2603	1/1.22	781.60	797.93	6112	3108	1/0.51
P-NiCo$_2$S$_4$	856.46	874.01	7432	4884	1/0.66	781.71	797.84	16090	7534	1/0.47
NiCo$_2$S$_{4-x}$	856.29	873.74	3497	2128	1/0.60	781.80	797.91	8150	3164	1/0.38
P-NiCo$_2$S$_{4-x}$	856.14	873.49	8201	4323	1/0.52	782.02	798.04	18800	6097	1/0.32

Table S3. Comparative specific capacitance/capacity of the P-NiCo$_2$S$_{4-x}$ electrode and the recently-reported Ni/Co-based electrode materials.

Electrode materials	Morphological structure	Electrolyte	Current density	Specific capacitance (F g^{-1})	Ref.
NiCo$_2$S$_4$	nanorod	6 M KOH	1 A g^{-1}	1610	9
EC/NiCo$_2$S$_4$	nanosheet	1M KOH	1 A g^{-1}	1394	10
C/NiCo$_2$S$_4$	nanosphere	6 M KOH	2 A g^{-1}	1545	11
P-NiCo$_2$S$_4$	nanotube	6 M KOH	1 A g^{-1}	2080	12
NiCo$_2$O$_4$@GQDs	nanosheet	2M KOH	1 A g^{-1}	1382	13
Co$_9$S$_8$@NiCo$_2$O$_4$	nanoneedle/nanosheet	3M KOH	1 A g^{-1}	1966	14
NiCo$_2$O$_4$	hexagonal nanostructure	3M KOH	1 A g^{-1}	1525	15
NiCo$_2$S$_4$@CoS$_2$	Nanosheet/nanowire	2M KOH	1 A g^{-1}	1565	16
NiCo$_2$S$_4$	nanoflake	6 M KOH	2.5A g^{-1}	2141.9	17
CoNi$_2$S$_4$	nanosheet	6 M KOH	2 A g^{-1}	2235	18
Our work	nanotube	2M KOH	1 A g^{-1}	3012	–

Note: To obtain a reasonable comparison with previous reports, the corresponding specific capacitance (C$_p$, F g^{-1}) of P-NiCo$_2$S$_{4-x}$ was calculated using the following equation:

$$C_s = 2\frac{I\int_{t_i}^{t_f} V dt}{m\Delta V^2}$$

(8)

Accordingly, the specific capacitance of the P-NiCo$_2$S$_{4-x}$ electrode was determined to be 3012 F g^{-1} at 1 A g^{-1}.

References

1. G. Kresse and J. Furthmüller, *Physical review B*, 1996, **54**, 11169.

2. J. Hu, X. Ma, W. Duan, Z. Liu, T. Liu, H. Lv, C. Huang, L. Miao and J. Jiang, *ACS Applied Nano Materials*, 2020, **3**, 7704-7712.

3. J. P. Perdew, K. Burke and M. Ernzerhof, *Phys. Rev. Lett.*, 1996, **77**, 3865.

4. S. Xiang and H. Huang, *Appl. Phys. Lett.*, 2008, **92**, 101923.

5. J. Hu, G. Ji, X. Ma, H. He and C. Huang, *Appl. Surf. Sci.*, 2018, **440**, 35-41.

6. H. Liang, C. Xia, Q. Jiang, A.N. Gandi, U. Schwingenschlögl and H.N. Alshareef, *Nano Energy*, 2017, **35**, 331–340.

7. S. Liu, Y. Yin, D. Ni, K.S. Hui, K.N. Hui, S. Lee, C.-Y. Ouyang and S.C. Jun, *Energy Storage Mater.*, 2019, **19**, 186–196.

8. S. Surendran, S. Shanmugapriya, A. Sivanantham, S. Shanmugam and R.K. Selvan, *Adv. Energy Mater.*, 2018, **8**, 1800555.

9. M. Zhou, H. Zhao, F. Ko, P. Servati, A. Bahi, S. Soltanian, F. Ge, Y. Zhao and Z. Cai, *J. Power Sources*, 2019, **440**, 227146.

10. Y. Liu, Z. Li, L. Yao, S. Chen, P. Zhang and L. Deng, *Chem. Eng. J.*, 2019, **366**, 550–559.

11. W. Lu, M. Yang, X. Jiang, Y. Yu, X. Liu and Y. Xing, *Chem. Eng. J.*, 2020, **382**, 122943.

12. H. Gu, W. Fan and T. Liu, *Nanoscale Horiz.*, 2017, **2**, 277–283.

13. J. Luo, J. Wang, S. Liu, W. Wu, T. Jia, Z. Yang, S. Mu and Y. Huang, *Carbon*, 2019, **146**, 1–8.

14. Q. Liu, X. Hong, X. Zhang, W. Wang, W. Guo, X. Liu and M. Ye, *Chem. Eng. J.*,

2019, **356**, 985–993.

15. J. Bhagwan, G. Nagaraju, B. Ramulu, S. C. Sekhar and J.S. Yu, *Electrochim. Acta*, 2019, **299**, 509–517.

16. M. Govindasamy, S. Shanthi, E. Elaiyappillai, S. Wang, P.M. Johnson, H. Ikeda, Y. Hayakawa, S. Ponnusamy and C. Muthamizhchelvan, *Electrochim. Acta*, 2019, **293**, 328–337.

17. F. Lu, M. Zhou, W. Li, Q. Weng, C. Li, Y. Xue, X. Jiang, X. Zeng, Y. Bando and D. Golberg, *Nano Energy*, 2016, **26**, 313–323.

18. Z. Li, D. Zhao, C. Xu, J. Ning, Y. Zhong, Z. Zhang, Y. Wang and Y. Hu, *Electrochim. Acta*, 2018, **278**, 33–41.